

Combined experimental-theoretical study of electron mobility-limiting mechanisms in SrSnO₃

Tristan K. Truttmann¹[✉], Jin-Jian Zhou², I-Te Lu², Anil Kumar Rajapitamahuni¹, Fengdeng Liu¹, Thomas E. Mates³, Marco Bernardi²[✉] & Bharat Jalan¹[✉]

The discovery and development of ultra-wide bandgap (UWBG) semiconductors is crucial to accelerate the adoption of renewable power sources. This necessitates an UWBG semiconductor that exhibits robust doping with high carrier mobility over a wide range of carrier concentrations. Here we demonstrate that epitaxial thin films of the perovskite oxide Nd_xSr_{1-x}SnO₃ (SSO) do exactly this. Nd is used as a donor to successfully modulate the carrier concentration over nearly two orders of magnitude, from $3.7 \times 10^{18} \text{ cm}^{-3}$ to $2.0 \times 10^{20} \text{ cm}^{-3}$. Despite being grown on lattice-mismatched substrates and thus having relatively high structural disorder, SSO films exhibited the highest room-temperature mobility, $\sim 70 \text{ cm}^2 \text{ V}^{-1} \text{ s}^{-1}$, among all known UWBG semiconductors in the range of carrier concentrations studied. The phonon-limited mobility is calculated from first principles and supplemented with a model to treat ionized impurity and Kondo scattering. This produces excellent agreement with experiment over a wide range of temperatures and carrier concentrations, and predicts the room-temperature phonon-limited mobility to be $76\text{--}99 \text{ cm}^2 \text{ V}^{-1} \text{ s}^{-1}$ depending on carrier concentration. This work establishes a perovskite oxide as an emerging UWBG semiconductor candidate with potential for applications in power electronics.

¹Department of Chemical Engineering and Materials Science, University of Minnesota, Minneapolis, MN 55455, USA. ²Department of Applied Physics and Materials Science, California Institute of Technology, Pasadena, CA 91125, USA. ³Materials Department, University of California, Santa Barbara, Santa Barbara, CA 93106, USA. ✉email: trutt009@umn.edu; bmarco@caltech.edu; bjalan@umn.edu

The application-driven discovery of functional materials is a high-risk, high-reward undertaking. Few materials reach commercial production for their intended application, but when they do, the payoff can be tremendous. For example, the discovery and subsequent application of GaN in blue light-emitting diodes (LEDs) and laser diodes has touched every aspect of the human experience from providing a low-cost affordable alternative to indoor lighting to its use in high-density recording media and full-color LCD display backlights. But materials discovery often suffers from major drawbacks. In the example of blue LEDs, GaN lacked lattice-matched substrates and failed to show p-type conductivity upon early doping attempts¹. These challenges deterred the vast majority of LED researchers, who instead opted to study II–VI semiconductors which—despite obvious degradation problems—were attractive because they could easily be grown with high structural quality, achieve ambipolar doping, and be made into working devices—albeit short-lived ones².

The ongoing search for ultra-wide bandgap (UWBG, $E_g > 4$ eV) semiconductors closely echoes the early stage of blue LED research, and it is motivated by the need for a semiconductor that can deliver efficient and compact switching for power conversion. The binary oxide β -Ga₂O₃ is winning the field's attention due in part to—much like II–VI semiconductors—the commercial availability of large-area single-crystal lattice-matched substrates. This, and the material's chemical simplicity, make β -Ga₂O₃ an attractive material system for large-area device fabrication while also eliminating the obstacles of mismatch-induced dislocations and cation nonstoichiometry. While β -Ga₂O₃ provides a robust platform for working devices, there remain several materials that may, if carefully investigated, present excellent prospects as UWBG semiconductors.

This work explores the mobility-limiting mechanisms in one such under-investigated UWBG semiconductor, SrSnO₃ (SSO), by combining experiments and computation. SSO is a perovskite oxide with a bandgap of 4.1–4.6 eV^{3–6}. Much like the well-studied perovskite BaSnO₃, SSO's conduction band is heavily derived from Sn 5s orbitals, which results in a relatively low electron effective mass of $m^* = 0.4 m_e$ ^{7,8}. This property has been exploited in La-doped thin films grown by pulsed laser deposition (PLD) to produce films with room-temperature electron mobilities as high as 55.8 cm² V⁻¹ s⁻¹^{6,9–13}. Transistors have also been produced using SSO as a channel material^{14–17} and improvements in fabrication have been made by optimizing ohmic metal contacts to SSO¹⁸. These promising results in a relatively new material system beg the question: what is the fundamental mobility limit of SSO? Ideally, this question should be answered with a joint effort

in experiment and computation. However, experimental studies showing robust controllable doping of SSO are lacking, preventing this question from being directly addressed. Of the SSO films grown by PLD, the best dopant activation reported was 70% of the La dopants which was only possible after post-growth annealing⁶. In previous work, we showed a 1:1 correspondence between La dopants and charge carriers using secondary ionization mass spectrometry (SIMS) on 48 nm of MBE-grown SSO. However, thinner 12 nm films were shown to be compensated¹⁹. In a later work, we showed that the surface was responsible for this compensation, which can be negated by growing thicker films²⁰. In this work, we systematically explore doping in SSO films exceeding 200 nm. By showing excellent doping control over nearly two orders of magnitude in carrier concentration, and using state-of-the-art calculations to investigate the mobility of SSO from first-principles, we establish SSO as a strong candidate UWBG semiconductor. SSO thin films achieve higher carrier concentrations, higher conductivity, and higher mobility at high carrier concentrations than the leading UWBG semiconductor β -Ga₂O₃. First-principles calculations of electron–phonon (e–ph) interactions, charge transport, and polaron effects provide a quantitative analysis of electrical transport in this semiconductor, calculating the room-temperature phonon-limited mobility at 76–99 cm² V⁻¹ s⁻¹.

Results and discussion

Successful n-type doping with Nd. A series of samples with the structure shown in Fig. 1a were grown using hybrid molecular beam epitaxy (MBE) with identical conditions except varying the Nd effusion cell temperature T_{Nd} . Structural characterization using high-resolution X-ray diffraction (HR-XRD) confirmed phase-pure, epitaxial SSO films as shown in Supplementary Figure 1. SIMS was also performed on these samples using a Nd-implanted standard as calibration. However, as explained in detail in Supplementary Note 1, the many abundant isotopes of Nd make the SIMS results unreliable. Therefore, we rely on the relationship between the carrier concentration from Hall measurements and the Nd flux at the crucible orifice to infer the dopant activation. The Nd flux at the crucible orifice can be calculated from the kinetic theory of gases:

$$\text{Nd flux at orifice} = \frac{P}{\sqrt{2\pi mk_B T_{\text{Nd}}}}$$

Where P is the equilibrium vapor pressure of Nd calculated with parameters from Alcock et al.²¹, m is the mass of a Nd atom, and k_B is the Boltzmann constant. Fig. 1b shows room-temperature carrier concentrations n_{RT} as a function of the Nd flux at the crucible

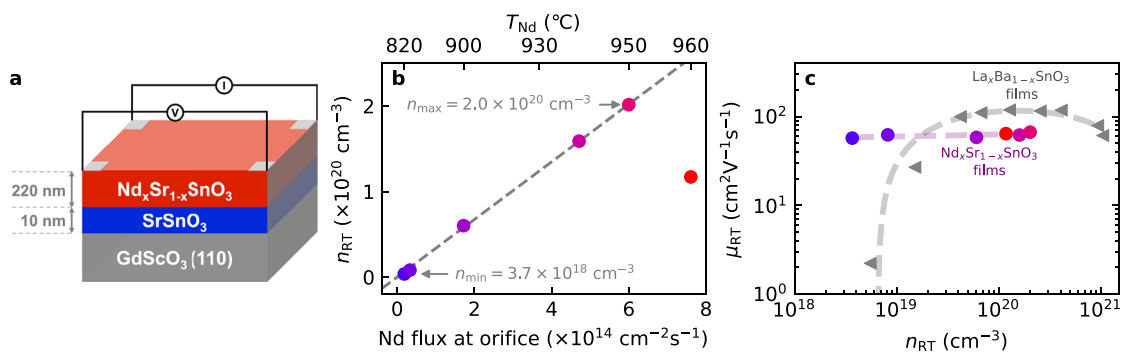


Fig. 1 Room-temperature electronic transport properties of Nd_xSr_{1-x}SnO₃ films. **a** Schematic of the sample structure. **b** Plot showing the room-temperature carrier concentration (n_{RT}) from van der Pauw measurements as a function of the equilibrium Nd flux at the crucible orifice. **c** Room-temperature mobility (μ_{RT}) of Nd_xSr_{1-x}SnO₃ (SSO) films (as circles) compared to La_xBa_{1-x}SnO₃ thin films (as triangles) grown using the same radical-based hybrid molecular beam epitaxy method²⁶. In all plots, the SSO marker color indicates the Nd effusion cell temperature.

orifice. For a series with 100% dopant activation, n_{RT} vs. Nd flux at the orifice should follow a straight line with an intercept of zero. We find that all samples with $T_{Nd} \leq 950$ °C follow this trend with higher T_{Nd} leading to lower carrier concentrations. This behavior suggests 100% dopant activation with a doping limit of $n_{max} = 2.0 \times 10^{20}$ cm⁻³ similar to the results found for La:SSO¹⁹. In principle, a similar behavior could also be produced by a series where each sample has exactly the same dopant activation <100%. In practice, however, samples with <100% activation have activation percentages with a strong dependence on dopant concentration^{6,22,23}, and therefore, should not yield a linear dependence. In fact, there are well-established theoretical explanations for this behavior²⁴. For this reason, although not directly, the observed behavior is a strong evidence of 100% activation in our samples. We note that Wei et. al. have reported slightly higher concentrations of 3.6×10^{20} cm⁻³ in La:SSO, which might be explained by their lower substrate temperature of 790 °C⁶. We also note that similarly high electron mobilities can be achieved in SSO grown by traditional ozone MBE (private communication with Prof. Darrell G. Schlom, 2021). The lower limit $n_{min} = 3.7 \times 10^{18}$ cm⁻³ is the lowest carrier concentration achieved to-date in conductive SSO, and it approaches Mott's critical carrier concentration of 1.4×10^{18} cm⁻³, assuming an electron effective mass $m^* = 0.4 m_e$ ^{7,8} and a static dielectric constant $\epsilon = 17.8$ ²⁵. We show in Fig. 1c the room-temperature electron mobility (μ_{RT}) of these samples vs. n_{RT} . Also shown for comparison are results for La_xBa_{1-x}SnO₃ (La:BSO) grown using the same radical-based hybrid MBE method²⁶. The mobility of BSO is strongly dependent on carrier concentration and this dependence is attributed to the presence of charged dislocations as the dominant electron scattering mechanism^{26,27}. Conversely, the SSO mobility is nearly independent of carrier concentration, with only a slight positive slope with increasing carrier density, suggesting an altogether different dominant scattering mechanism in SSO.

Temperature-dependent transport in SSO. To explore the mobility-limiting mechanisms in SSO, we measure temperature-dependent transport, as shown in Fig. 2. The data from the highest-doped sample—the one above the doping limit—was excluded for clarity. The resistivity vs temperature data in Fig. 2a and the temperature-independent carrier concentrations in Fig. 2b confirm that all the samples behave as degenerately doped semiconductors. Although the two lightest-doped samples show a resistivity minimum near 150 K, we show in Supplementary Fig. 2 that these two samples' resistivities have a temperature dependence consistent with Kondo scattering^{28,29} suggesting that Nd³⁺ serves not only as a shallow donor, but also as a magnetic impurity. This result is not surprising given the unpaired *f*-electrons in Nd³⁺ (electron configuration [Xe]4f³5d⁰6s⁰) and the paramagnetism observed from Nd³⁺ impurities in structurally similar BSO^{30,31}. The small downturn in carrier concentration below 25 K seen for the two lightest-doped samples is an artifact due to Aronov–Altshuler electron–electron interaction (EEI)³², so

although the EEI is present in these two samples, it only manifests as an increase in the Hall coefficient below 25 K where the resistance is already saturated.

The temperature-dependent mobility (μ) for these samples is shown in Fig. 2c. At low temperatures, there is a divergent behavior where the mobility of the lightest-doped samples increases with increasing temperature, while most samples show a monotonic decrease with temperature. At high temperatures, all samples have very similar mobilities that monotonically decrease with temperature. This mobility decrease is indicative of phonon scattering, and the similarities among samples with vastly different doping concentrations suggest that phonon scattering is the predominant mobility-limiting mechanism in SSO at room temperature. To understand the mobility-limiting mechanisms in SSO, we employ first-principles calculations (see “Methods” section) to study e–ph scattering processes and calculate the phonon-limited mobility as a function of temperature.

Electron–phonon interaction in SSO. Figure 3a shows the phonon dispersion curves in SSO along several high-symmetry lines in the Brillouin zone (BZ). Unlike perovskite oxides with simple cubic structure, such as SrTiO₃ (STO), the phonon dispersions in SSO are quite complicated due to the structural distortion to orthorhombic symmetry, which leads to a large unit cell with 20 atoms. Each phonon branch in the simple cubic structure transforms into four branches in the orthorhombic structure due to BZ folding, resulting in 3 acoustic and 57 optical branches. We denote the four phonon branches above 80 meV as LO-1 and the four branches between 50 and 60 meV as LO-2 phonons; they correspond, respectively, to the highest and second-highest LO branches in the undistorted cubic perovskite structure³³. The color scale on the phonon dispersions shown in Fig. 3a characterizes the e–ph coupling strength (in log scale) between different phonon modes and the electronic state at the conduction band minimum (CBM). Similar to cubic STO, the LO-1 and LO-2 phonons exhibit the strongest coupling with electrons due to the long-range Frohlich e–ph interaction^{34–37}. Figure 3b, c shows the displacement patterns of the LO-1 and LO-2 phonons, respectively, in the long-wavelength limit. Both branches can be described as distortions of the SnO₆ octahedra, with LO-1 phonons corresponding to stretching and LO-2 phonons to bending of the Sn–O bonds.

Figure 3d shows the calculated e–ph scattering rates (Γ) at room temperature with a carrier concentration of 3.7×10^{18} cm⁻³. The scattering rates are separated into the contributions from LO-1, LO-2, and all other phonon modes. Figure 3d also shows the transport distribution function (TDF) which quantifies the contribution to the conductivity of electrons with a given energy—here the energy range of interest is primarily within 100 meV of the CBM. In this energy range, LO-2 and other phonons modes (except LO-1) give the strongest contributions to electron scattering. This trend is in noticeable contrast to the well-known

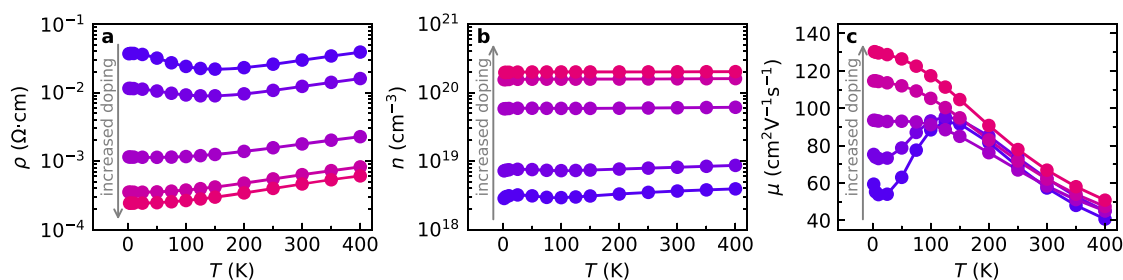


Fig. 2 Temperature-dependent transport data of Nd_xSr_{1-x}SnO₃ films. **a** Resistivity ρ , **b** carrier density n , and **c** mobility μ as a function of temperature. The color indicates Nd effusion cell temperature.

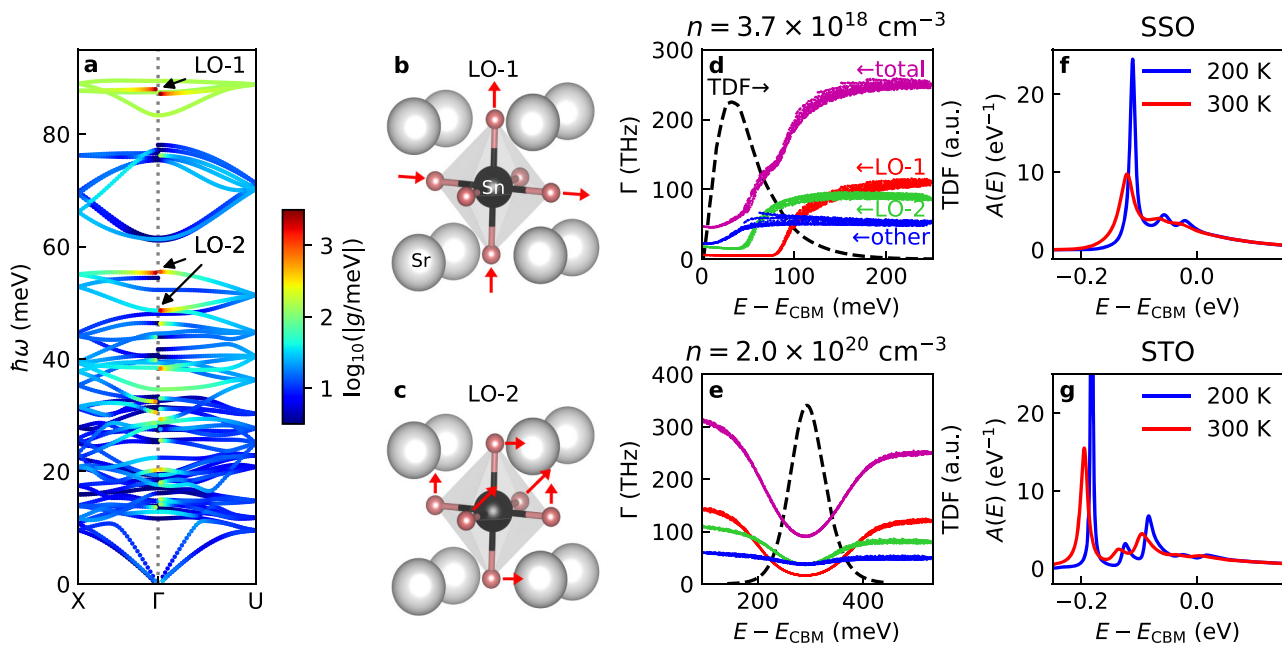


Fig. 3 Calculations of electron-phonon interactions in SrSnO_3 . **a** Phonon dispersions overlaid with a log-scale color map of the electron-phonon (e-ph) coupling strength $|g_v(k=G, q)|$. **b, c** The atomic displacement patterns of the first longitudinal optical phonon branch of the parent cubic unit cell (LO-1) (**a**) and second longitudinal optical phonon branch of the parent cubic unit cell (LO-2) (**b**), the phonon modes that exhibit the strongest coupling with electrons. **d** Total and mode-resolved e-ph scattering rates (Γ) in SrSnO_3 (SSO), computed at 300 K and $n = 3.8 \times 10^{18} \text{ cm}^{-3}$. The black dashed line is the transport distribution function (TDF) which quantifies the contribution to transport from electronic states at a given energy. **e** The scattering rates and TDF for SSO doped into the degenerate regime with $n = 2.0 \times 10^{20} \text{ cm}^{-3}$. **f** Electron spectral function for the conduction band minimum (CBM) in SSO computed using the ab initio cumulant approach at temperatures of 200 and 300 K, and a carrier concentration of $n = 3.8 \times 10^{18} \text{ cm}^{-3}$. For comparison, the electron spectral function in STO at 200 K is shown in **g**. The zero of the electron energy (E) axis in **d-g** is the energy of the CBM.

perovskite semiconductor STO and other transition metal oxides, where only LO-1 and LO-2 are the main contributors to electron scattering due to their dominant Frohlich interaction³³. This result points to the possibility of engineering higher mobility in SSO by fine-tuning the octahedral rotations and distortions, which are ultimately responsible for the BZ folding resulting in a large number of optical modes with 10–40 meV energy that limit the mobility.

The e-ph scattering rates are also shown for the degenerate doping regime with a carrier concentration of $2.0 \times 10^{20} \text{ cm}^{-3}$ in Fig. 3e. Although the scattering rates and TDF show a qualitatively different dependence on energy—troughing and peaking at the Fermi energy, respectively—the conclusion drawn from these data are unchanged from those at lower carrier concentration, namely that both LO-2 and other phonon modes (except LO-1) make significant contributions to the e-ph scattering.

In many oxides with ionic bonds, the e-ph coupling is strong enough to induce polaron effects³⁸, whose treatment goes beyond the limit of weak e-ph interaction and band transport presented above. The electron spectral function, which describes the density of states of an electron in a given electronic state, can quantify such higher-order e-ph processes and polaron effects. Figure 3f shows the electron spectral function, as a function of electron energy E , for a state near the CBM in SSO, calculated using our cumulant approach³⁷. In semiconductors with weak e-ph coupling, the spectral function exhibits only a single quasiparticle peak, whose width is proportional to the e-ph scattering rate. In ionic semiconductors and insulators with noticeable polaron effects, however, the spectral function may exhibit multiple peaks, including the original quasiparticle peak and one or more phonon satellites separated from the quasiparticle peak by the energy of the phonons with the strongest e-ph coupling³⁷. The presence of

these satellites is a signature of strong e-ph coupling, and is typically due to the coupling of electrons with LO phonons via the Frohlich interaction. The integral of the spectral function outside the quasiparticle peak (the so-called satellite spectral weight) is a measure of the strength of polaron effects and of the deviation of the transport mechanism from the conventional band transport regime³⁷. The 200 K spectral function in SSO, shown in Fig. 3f, exhibits a sharp quasiparticle peak and weak sidebands due to the LO-1 and LO-2 modes; the main peak broadens at 300 K, but the overall weight of the polaron sidebands is still less than ~20%. For comparison, the spectral function in STO, shown in Fig. 3g, has a polaron sideband spectral weight of order 50% over a wide temperature range³⁷. The weak polaron effect in SSO, which is partially responsible for its relatively high room-temperature mobility, is due to both the extended *s*-orbital character of the conduction band and the relatively weak Frohlich interaction between electrons and LO phonons in SSO due to the weaker ionic character of its bonds compared to STO (as quantified by smaller Born charges). By contrast, in STO the bonds are more strongly ionic and the conduction bands have *d*-orbital character, thus exhibiting both a smaller band velocity and a stronger overall Frohlich e-ph interaction and polaron effects.

First-principles mobility calculations. To clarify the microscopic origin of the room-temperature mobility, we carry out first-principles calculations of the temperature-dependent mobility of SSO, separately for each of the carrier concentrations investigated experimentally. The phonon-limited mobilities, which account for scattering from all phonon modes, are plotted as a function of temperature in Fig. 4a. The calculated room-temperature phonon-limited mobilities are 76–99 $\text{cm}^2 \text{ V}^{-1} \text{ s}^{-1}$ depending on carrier concentration. This dependence on carrier concentration

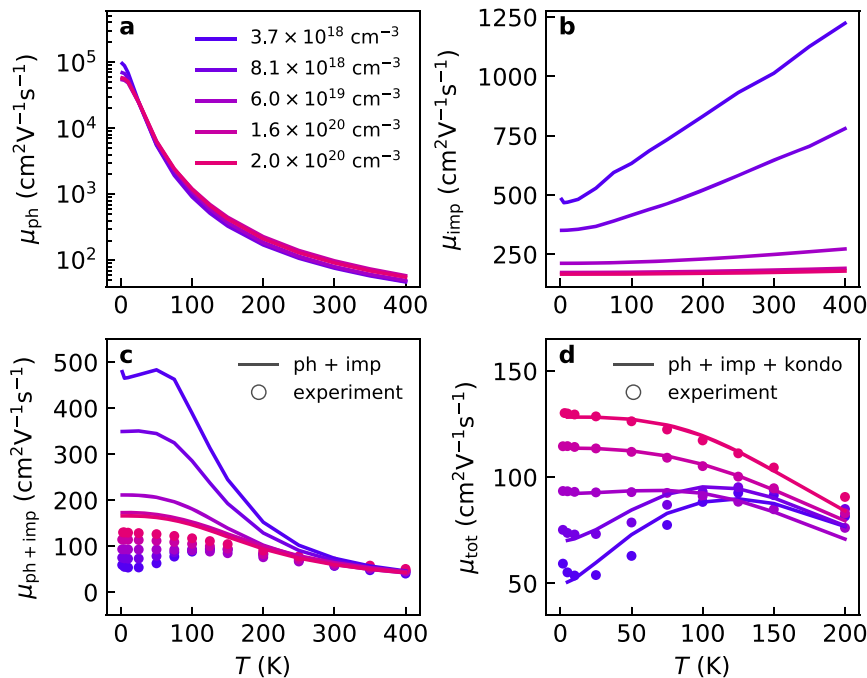


Fig. 4 Comparing experimental and calculated electron mobilities in $\text{Nd}_x\text{Sr}_{1-x}\text{SnO}_3$ films. **a** Computed phonon-limited electron mobility as a function of doping, obtained by solving the Boltzmann transport equation with ab initio electron–phonon (e–ph) scattering. **b** Computed defect-limited carrier mobility using the effective mass model. **c** The computed carrier mobility, including scattering from phonons and ionized impurities, compared to the experimental data shown as symbols. **d** Comparison of the computed carrier mobility—including the effects from phonons, ionized impurities, and Kondo scattering—with the experimental data shown as symbols.

is due to the change of scattering phase space for e–ph processes as a function of carrier concentration.

The effect of the Nd dopants is included on top of the first-principles calculations using an effective mass model for ionized impurity scattering, as shown in Fig. 4b. Lower carrier concentrations show a stronger temperature dependence, because the Fermi level is near the band edge where the relaxation times due to ionized impurity scattering depend strongly on carrier energy ($\tau \propto E^{3/2}$). For the lower carrier concentrations, as temperature increases, the occupation probability above the band edge increases, leading to a strongly temperature-dependent carrier mobility. The mobilities from Fig. 4a–c are combined using Matthiessen’s rule, and the resulting mobility is compared to the experimental values in Fig. 4c. The computed mobilities match the experimental results exceptionally well at higher temperatures (>250 K), where the mobility is phonon limited and nearly independent of carrier concentration, but deviate from the experiment at low temperatures, especially for samples with low carrier concentrations. This discrepancy can be explained by Kondo scattering from Nd acting as a magnetic impurity.

To account for Kondo scattering, the residual from Fig. 4c is fit to an empirical expression for Kondo scattering obtained by Costi et al.³⁹ and later fit to an empirical expression by Goldhaber-Gordon et al.^{40,41}:

$$\mu_K(T) = \mu_{K0} \left(1 + \left(2^{1/S} - 1 \right) \left(\frac{T}{T_K} \right)^2 \right)^S \quad (1)$$

We vary the prefactor μ_{K0} and the Kondo temperature T_K , and fix the spin parameter S to the theoretical value $S = 0.225$ in Goldhaber-Gordon et al.⁴⁰. The final mobility results—including phonon scattering, ionized impurity scattering, and Kondo scattering—are compared to experiment in Fig. 4d. The theoretical results closely match experiment for every sample. One feature that is not captured by the model is the small upturn

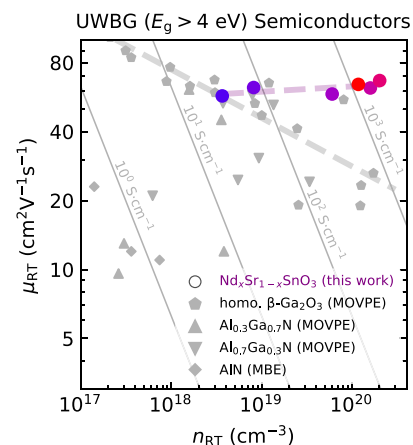


Fig. 5 Comparison to other ultra-wide bandgap (UWBG) semiconductors.

A comparison of the room-temperature Hall mobilities of $\text{Nd}_x\text{Sr}_{1-x}\text{SnO}_3$ (SSO) compared to the best-reported mobilities of other ultra-wide bandgap semiconductor thin films showing SSO’s superior mobility and conductivity above 10^{19} cm^{-3} . The highest conductivity achieved in SSO from has been included from Wei et al.⁶. Data for homoepitaxial gallium oxide grown by metal-organic vapor phase epitaxy (MOVPE) are from Baldini et al.²⁷. A gray dashed line has been added as a guide to the eye. Aluminum gallium nitride grown by MOVPE and aluminum nitride data grown by molecular beam epitaxy (MBE) are from refs. 28–33.

in μ below 25 K which, as explained earlier, is an artifact of EEI which was not accounted for in our calculations.

Comparison to other UWBG semiconductors. To benchmark SSO as an UWBG semiconductor, we show in Fig. 5 room-temperature mobilities at different carrier concentrations in our

SSO films along with their conductivities as a contour plot. For comparison, we include the highest conductivity values to date from thin films of well-known UWBG semiconductors, including β -Ga₂O₃ and Al_xGa_{1-x}N (AlGaN) for $x = 0.3, 0.7$, and $1^{22,23,42-46}$. It is noteworthy that our doped SSO films show high conductivity of 2157 S cm⁻¹ while maintaining a reasonably high electron mobility of 67 cm² V⁻¹ s⁻¹ combined with a high carrier density, 2×10^{20} cm⁻³. We note that other UWBG semiconductors, such as AlGaN, can also achieve high mobilities (426 cm² V⁻¹ s⁻¹ at a carrier density of 7.3×10^{14} cm⁻³) or high carrier concentrations (3.4×10^{19} cm⁻³ with electron mobility of 24 cm² V⁻¹ s⁻¹), but these properties cannot be achieved simultaneously^{43,47}. Similarly, β -Ga₂O₃ films can achieve high room-temperature mobilities, 184 cm² V⁻¹ s⁻¹ at 3.2×10^{15} cm⁻³⁴⁸, or higher carrier concentrations of 1.7×10^{20} cm⁻³ but with lower mobility of 25 cm² V⁻¹ s⁻¹⁴⁹. In this context, our early attempt yielding record high mobilities with high carrier concentrations in perovskite SSO is especially promising. These results are particularly encouraging given that our SSO films were grown on lattice-mismatched substrates and have a high level of structural disorder as shown by rocking curves in Supplementary Fig. 1 and the full width at half-maximum values in Supplementary Table 1.

However, the success of an UWBG semiconductor requires more than just high conductivity. In particular, high mobilities should be maintained well into the non-degenerate doping regime, ideally below 10^{16} cm⁻³. The lowest concentration we could achieve in this work was 3.7×10^{18} cm⁻³. It is unclear what prevented us from achieving conductivity at lower concentrations, but one likely culprit is the high structural disorder seen in rocking curves. Future work should focus on improving structural quality by producing lattice-matched substrates to SSO.

Another desirable quality for UWBG semiconductors is p-type doping. Many of the leading UWBG semiconductors are not amenable to p-type doping due to the prohibitively high activation energies or the formation of self-trapped holes⁵⁰⁻⁵². At this early stage, it is unclear whether or not SSO supports p-type doping. But success in p-type doping of the related perovskite stannate BaSnO₃ with K⁵³ and N⁵⁴ is encouraging for the prospects of p-type SSO. Future work should attempt similar doping strategies in SSO.

In summary, we have established perovskite SSO as an emerging candidate UWBG semiconductor through a joint effort of experiment and theory. The combination of controlled doping and detailed transport measurements with first-principles calculations of e-ph scattering and charge transport allowed us to understand and predict the transport behavior and mobility-limiting mechanisms in SSO.

Methods

Film growth and characterization. All samples were grown with a radical-based hybrid MBE approach. The reader is referred to previous publications for a detailed description of the method^{55,56}, but a brief description is provided here. Single-crystal 5 mm × 5 mm GdScO₃ (110) (CrysTec GmbH, Germany) were chosen as substrates for these films. This substrate choice was motivated by being the commercially available perovskite oxide substrate with the best lattice match ($\epsilon_m = -1.6\%$) with SSO films. It is also insulating and has the same Pbnm space group as SSO. For more information about substrate choice, the reader is directed to our previous works on the strain engineering of SSO⁸ and strain relaxation of SSO films²⁰. The substrates were heated to 950 °C (thermocouple temperature) in the hybrid MBE system (Scienta Omicron, Germany). Growth was preceded by 20 minutes of oxygen cleaning via 250 W RF oxygen plasma that achieves a background oxygen pressure of 5×10^{-6} Torr (Mantis, UK). Strontium and neodymium were provided via thermal sublimation from an effusion cell. Strontium was supplied at 444 °C to achieve a beam equivalent pressure (BEP) of 2.4×10^{-8} Torr, whereas the neodymium effusion cell temperature was varied to control the dopant concentration. Tin was supplied by a radical-initiating chemical precursor hexamethylditin (HMDT) which offers both high volatility and high oxygen reactivity to help achieve cation and oxygen stoichiometry, respectively. HMDT

was supplied at a BEP of 2×10^{-6} Torr. During growth, oxygen was supplied by the same oxygen plasma parameters that were used for oxygen cleaning. These conditions achieved a growth rate of 55 nm h⁻¹. A 10 nm undoped buffer layer was used, motivated by its success in improving the mobility of the related material BaSnO₃²⁶ although its efficacy has not yet been tested in SSO. High-resolution X-ray diffraction (HR-XRD) data were collected with a PANalytical X'Pert Pro thin film diffractometer with a Cu parabolic mirror and germanium 4-bounce monochromator. All transport data were collected in the van der Pauw geometry in the temperature- and magnetic field-controlled environment provided by a DynaCool physical property measurements system, (Quantum Design, USA). The magnetic field was swept between ± 9 T.

Dynamic SIMS was performed on the Cameca IMS 7f-Auto at UC Santa Barbara. Ion implantation was performed on the undoped sample at Innovion Corporation (California, USA) to serve as a calibration sample. An O²⁺ primary beam was rastered across a 150 μ m × 150 μ m square to etch a trench into the film and produce secondary ions from which a 62 μ m-diameter circle in the center of the trench was analyzed. All analyzed samples were coated in Au/Pt and an electron flood gun was used to minimize charging. Double focusing magnetic sector optics was used to filter secondary ions which used an electrostatic energy filter with a window width set to 150 eV followed by an electromagnet mass filter. The mass corresponding to ¹¹⁶Sn was chosen as the matrix signal.

Calculations of electron-phonon interactions and electron mobility. We carried out ab initio calculations on orthorhombic SSO with experimental lattice constants ($a = 5.7093$ Å, $b = 5.7053$ Å, $c = 8.0676$ Å). The ground-state electronic structure was computed using density functional theory (DFT) with the Quantum ESPRESSO code⁵⁷. We employed the PBEsol-GGA exchange-correlation functional and norm-conserving pseudopotentials from PseudoDojo⁵⁸. The kinetic energy cutoff for the plane-wave basis was set to 90 Ry. We use density functional perturbation theory (DFPT) to compute the lattice dynamical properties and obtain the e-ph matrix elements on electronic $8 \times 8 \times 6$ k-point and phonon $4 \times 4 \times 3$ q-point coarse grids using the Perturbo code³⁶. The e-ph matrix elements were interpolated on finer Brillouin zone grids of up to $100 \times 100 \times 80$ and employed to compute the e-ph scattering rates. The phonon-limited electron mobility was computed by iteratively solving the linearized Boltzmann transport equation with ab initio e-ph collisions³⁶. The electron spectral functions were computed using a finite-temperature cumulant approach we recently proposed³⁷.

The ionized impurity scattering mobility m_{imp} was calculated using an effective mass model that uses an energy-dependent transport relaxation time τ_1 due to ionized impurity scattering⁵⁹

$$\mu_{\text{imp}} = \frac{e \tau_1 E}{m^* E} \quad (2)$$

where e is the electron charge, m^* is the electron effective mass, and E is the electron energy. The thermal average A , where A is a physical quantity of interest, is defined as

$$A = \int_0^\infty dE A(E)g(E)f(E, E_f) \quad (3)$$

The density of states $g(E)$ was calculated from the effective mass assuming perfect band parabolicity:

$$g(E) = \frac{2^{1/2} m^{*3/2}}{\pi^2 \hbar^3} E^{1/2} \quad (4)$$

where \hbar is the reduced Planck constant. The Fermi energy E_f used in the Fermi-Dirac distribution $f(E, E_f)$ is calculated with an iterative method to match the carrier concentration n measured in the thin films:

$$n = \int_0^\infty dE g(E) f(E, E_f) \quad (5)$$

Here we assume that all the dopants are fully ionized, that is, the carrier concentration n is equal to the doping concentration N_i . The transport relaxation time due to ionized impurity scattering, τ_1 , is computed using:

$$\tau_1 = \frac{16\pi(2m^*)^{1/2} \epsilon_0^2 e^2}{e^4 N_i} E^{3/2} \left\{ \ln \left(1 + \frac{8m^* E}{\hbar^2 q_{\text{scr}}^2} \right) - \left(1 + \frac{\hbar^2 q_{\text{scr}}^2}{8m^* E} \right)^{-1} \right\}^{-1} \quad (6)$$

where ϵ_s is the static dielectric constant and N_i is the concentration of ionized impurities assumed to be equal to the carrier concentrations in these films. The screening vector q_{scr} is defined as

$$q_{\text{scr}}^2 = \frac{2^{1/2} m^{*3/2} e^2}{\pi^2 \hbar^3 \epsilon_0 \epsilon_s} \int_0^\infty dE E^{1/2} \left(-\frac{\partial f}{\partial E} \right) \quad (7)$$

The effective masses computed with DFT using the PBEsol functional are $m^* = 0.38 m_e$ along the a -direction and $m^* = 0.36 m_e$ along the c -direction, in very good agreement with the experimental value of $m^* = 0.4 m_e$ ^{7,8}. Further refining the computed effective masses using hybrid functional (HSE) calculations on orthorhombic SrSnO₃ (20 atoms per unit cell) would be demanding. Yet, we have verified that PBEsol and HSE calculations produce nearly identical effective masses and band dispersions in cubic SrSnO₃ (5 atoms in the unit cell), where HSE calculations are feasible. In cubic SrSnO₃, we found that the effective mass and the

dispersion of the lowest conduction band is nearly identical in HSE and PBEsol: the effective mass is $0.234 m_e$ in PBEsol and $0.250 m_e$ in HSE. This is strong evidence that our PBEsol calculations are not affected by any errors related to the effective mass in PBEsol.

Data availability

The data that support the findings of this study are available in the manuscript or its Supplementary Information. Other data are available from the corresponding authors (T.K.T. or B.J.) upon reasonable request.

Code availability

All code that was used to generate the findings of this study are available from the references within or otherwise are available from the authors upon reasonable request.

Received: 19 January 2021; Accepted: 22 October 2021;

Published online: 11 November 2021

References

1. Maruska, H. P. & Rhines, W. C. A modern perspective on the history of semiconductor nitride blue light sources. *Solid-State Electron.* **111**, 32–41 (2015).
2. Nakamura, S., Pearton, S. & Fasol, G. *The Blue Laser Diode: The Complete Story 2 edn* (Springer-Verlag, 2000).
3. Mizoguchi, H., Eng, H. W. & Woodward, P. M. Probing the electronic structures of ternary perovskite and pyrochlore oxides containing Sn^{4+} or Sb^{5+} . *Inorg. Chem.* **43**, 1667–1680 (2004).
4. Zhang, W., Tang, J. & Ye, J. Structural, photocatalytic, and photophysical properties of perovskite MSnO_3 ($M = \text{Ca}, \text{Sr}, \text{and Ba}$) photocatalysts. *J. Mater. Res.* **22**, 1859–1871 (2007).
5. Schumann, T., Raghavan, S., Ahadi, K., Kim, H. & Stemmer, S. Structure and optical band gaps of $(\text{Ba}, \text{Sr})\text{SnO}_3$ films grown by molecular beam epitaxy. *J. Vacuum Sci. Technol. A* **34**, 050601 (2016).
6. Wei, M. et al. High electrical conducting deep-ultraviolet-transparent oxide semiconductor La-doped SrSnO_3 exceeding $\sim 3000 \text{ S cm}^{-1}$. *Appl. Phys. Lett.* **116**, 022103 (2020).
7. Ong, K. P., Fan, X., Subedi, A., Sullivan, M. B. & Singh, D. J. Transparent conducting properties of SrSnO_3 and ZnSnO_3 . *APL Mater.* **3**, 062505 (2015).
8. Wang, T. et al. Engineering SrSnO_3 phases and electron mobility at room temperature using epitaxial strain. *ACS Appl. Mater. Interfaces* **10**, 43802–43808 (2018).
9. Baba, E. et al. Optical and transport properties of transparent conducting La-doped SrSnO_3 thin films. *J. Phys. D* **48**, 455106 (2015).
10. Liu, Q., Jin, F., Gao, G. & Wang, W. Ta doped SrSnO_3 epitaxial films as transparent conductive oxide. *J. Alloys Compd* **717**, 62–68 (2017).
11. Li, K., Gao, Q., Zhao, L. & Liu, Q. Transparent and conductive Sm-doped SrSnO_3 epitaxial films. *Optic. Mater.* **107**, 110139 (2020).
12. Li, K., Gao, Q., Zhao, L. & Liu, Q. Electrical and optical properties of Nb-doped SrSnO_3 epitaxial films deposited by pulsed laser deposition. *Nanoscale Res. Lett.* **15**, 164 (2020).
13. Wei, M., Cho, H. J. & Ohta, H. Tuning of the optoelectronic properties for transparent oxide semiconductor ASnO_3 by modulating the size of A-ions. *ACS Appl. Electron. Mater.* **2**, 3971–3976 (2020).
14. Chaganti, V. R. S. K., Prakash, A., Yue, J., Jalan, B. & Koester, S. J. Demonstration of a depletion-mode SrSnO_3 n-channel MESFET. *IEEE Electron Device Lett.* **39**, 1381–1384 (2018).
15. Chaganti, V. R. S. K., Truttmann, T. K., Liu, F., Jalan, B. & Koester, S. J. SrSnO_3 field-effect transistors with recessed gate electrodes. *IEEE Electron Device Lett.* **41**, 1428–1431 (2020).
16. Wei, M., Gong, L., Liang, D.-D., Cho, H. J. & Ohta, H. Fabrication and operating mechanism of deep-UV transparent semiconducting SrSnO_3 -based thin film transistor. *Adv. Electron. Mater.* **6**, 2000100 (2020).
17. Wen, J. et al. SrSnO_3 metal-semiconductor field-effect transistor with GHz operation. *IEEE Electron Device Lett.* **42**, 74–77 (2021).
18. Saran Kumar Chaganti, V. R. et al. Optimizing Ohmic contacts to Nd-doped n-type SrSnO_3 . *Appl. Phys. Lett.* **118**, 142104 (2021).
19. Truttmann, T., Prakash, A., Yue, J., Mates, T. E. & Jalan, B. Dopant solubility and charge compensation in La-doped SrSnO_3 films. *Appl. Phys. Lett.* **115**, 152103 (2019).
20. Truttmann, T. K., Liu, F., Garcia-Barriocanal, J., James, R. D. & Jalan, B. Strain relaxation via phase transformation in high-mobility SrSnO_3 films. *ACS Appl. Electron. Mater.* **3**, 1127–1132 (2021).
21. Alcock, C. B., Itkin, V. P. & Horrigan, M. K. Vapour pressure equations for the metallic elements: 298–2500K. *Can. Metall. Q.* **23**, 309–313 (1984).
22. Ive, T. et al. Controlled n-type doping of AlN:Si films grown on 6H-SiC(0001) by plasma-assisted molecular beam epitaxy. *Appl. Phys. Lett.* **86**, 024106 (2005).
23. Bryan, I. et al. Doping and compensation in Al-rich AlGaN grown on single crystal AlN and sapphire by MOCVD. *Appl. Phys. Lett.* **112**, 062102 (2018).
24. Weston, L., Bjaalie, L., Krishnaswamy, K. & Van de Walle, C. G. Origins of n-type doping difficulties in perovskite stannates. *Phys. Rev. B* **97**, 054112 (2018).
25. Petousis, I. et al. High-throughput screening of inorganic compounds for the discovery of novel dielectric and optical materials. *Sci. Data* **4**, 160134 (2017).
26. Prakash, A. et al. Wide bandgap BaSnO_3 films with room temperature conductivity exceeding 10^4 S cm^{-1} . *Nat. Commun.* **8**, 15167 (2017).
27. Mun, H. et al. Large effects of dislocations on high mobility of epitaxial perovskite $\text{Ba}_{0.96}\text{La}_{0.04}\text{SnO}_3$ films. *Appl. Phys. Lett.* **102**, 252105 (2013).
28. Kondo, J. Resistance minimum in dilute magnetic alloys. *Prog. Theor. Phys.* **32**, 37–49 (1964).
29. Lee, P. A. & Ramakrishnan, T. V. Disordered electronic systems. *Rev. Modern Phys.* **57**, 287–337 (1985).
30. McCalla, E., Phelan, D., Krogstad, M. J., Dabrowski, B. & Leighton, C. Electrical transport, magnetic, and thermodynamic properties of La-, Pr-, and Nd-doped $\text{BaSnO}_{3-\delta}$ single crystals. *Phys. Rev. Mater.* **2**, 084601 (2018).
31. Alaan, U. S. et al. Magnetism and transport in transparent high-mobility BaSnO_3 films doped with La, Pr, Nd, and Gd. *Phys. Rev. Mater.* **3**, 124402 (2019).
32. Yue, J., Thoutam, L. R., Prakash, A., Wang, T. & Jalan, B. Unraveling the effect of electron-electron interaction on electronic transport in La-doped SrSnO_3 films. *Appl. Phys. Lett.* **115**, 082102 (2019).
33. Zhou, J.-J., Hellman, O. & Bernardi, M. Electron-phonon scattering in the presence of soft modes and electron mobility in SrTiO_3 perovskite from first principles. *Phys. Rev. Lett.* **121**, 226603 (2018).
34. Fröhlich, H., Pelzer, H. & Zienau, S. Properties of slow electrons in polar materials. *London Edinburgh Dublin Philos. Mag. J. Sci.* **41**, 221–242 (1950).
35. Mahan, G. D. *Many-Particle Physics* 3 edn (Springer US, 2000).
36. Zhou, J.-J. et al. Perturbo: a software package for ab initio electron-phonon interactions, charge transport and ultrafast dynamics. *Comput. Phys. Commun.* **264**, 107970 (2021).
37. Zhou, J.-J. & Bernardi, M. Predicting charge transport in the presence of polarons: the beyond-quasiparticle regime in SrTiO_3 . *Phys. Rev. Res.* **1**, 033138 (2019).
38. Emin, D. *Polarons* (Cambridge University Press, 2012).
39. Costi, T. A., Hewson, A. C. & Zlatić, V. Transport coefficients of the Anderson model via the numerical renormalization group. *J. Phys.* **6**, 2519–2558 (1994).
40. Goldhaber-Gordon, D. et al. From the Kondo regime to the mixed-valence regime in a single-electron transistor. *Phys. Rev. Lett.* **81**, 5225–5228 (1998).
41. Lee, M., Williams, J. R., Zhang, S., Frisbie, C. D. & Goldhaber-Gordon, D. Electrolyte gate-controlled Kondo effect in SrTiO_3 . *Phys. Rev. Lett.* **107**, 256601 (2011).
42. Baldini, M. et al. Si- and Sn-doped homoepitaxial $\beta\text{-Ga}_2\text{O}_3$ layers grown by MOVPE on (010)-oriented substrates. *ECSS J. Solid State Sci. Technol.* **6**, Q3040 (2017).
43. Nakarmi, M. L., Kim, K. H., Zhu, K., Lin, J. Y. & Jiang, H. X. Transport properties of highly conductive n-type Al-rich $\text{Al}_x\text{Ga}_{1-x}\text{N}$ ($x \geq 0.7$). *Appl. Phys. Lett.* **85**, 3769–3771 (2004).
44. Collazo, R. et al. Progress on n-type doping of AlGaN alloys on AlN single crystal substrates for UV optoelectronic applications. *Phys. Status Solidi C* **8**, 2031–2033 (2011).
45. Borisov, B. et al. Si-doped $\text{Al}_x\text{Ga}_{1-x}\text{N}$ ($0.56 \leq x \leq 1$) layers grown by molecular beam epitaxy with ammonia. *Appl. Phys. Lett.* **87**, 132106 (2005).
46. Nam, K. B., Li, J., Nakarmi, M. L., Lin, J. Y. & Jiang, H. X. Achieving highly conductive AlGaN alloys with high Al contents. *Appl. Phys. Lett.* **81**, 1038–1040 (2002).
47. Taniyasu, Y., Kasu, M. & Makimoto, T. Increased electron mobility in n-type Si-doped AlN by reducing dislocation density. *Appl. Phys. Lett.* **89**, 182112 (2006).
48. Feng, Z., Anhar Uddin Bhuiyan, A. F. M., Karim, M. R. & Zhao, H. MOCVD homoepitaxy of Si-doped (010) $\beta\text{-Ga}_2\text{O}_3$ thin films with superior transport properties. *Appl. Phys. Lett.* **114**, 250601 (2019).
49. Leedy, K. D. et al. Highly conductive homoepitaxial Si-doped Ga_2O_3 films on (010) $\beta\text{-Ga}_2\text{O}_3$ by pulsed laser deposition. *Appl. Phys. Lett.* **111**, 012103 (2017).
50. Katsuragawa, M. et al. Thermal ionization energy of Si and Mg in AlGaN. *J. Cryst. Growth* **189–190**, 528–531 (1998).
51. Kyrtos, A., Matsubara, M. & Bellotti, E. On the feasibility of p-type Ga_2O_3 . *Appl. Phys. Lett.* **112**, 032108 (2018).
52. Galazka, Z. $\beta\text{-Ga}_2\text{O}_3$ for wide-bandgap electronics and optoelectronics. *Semicond. Sci. Technol.* **33**, 113001 (2018).
53. Kim, H. M., Kim, U., Park, C., Kwon, H. & Char, K. Thermally stable pn-junctions based on a single transparent perovskite semiconductor BaSnO_3 . *APL Mater.* **4**, 056105 (2016).
54. Wang, J. & Luo, B. Electronic properties of p-type BaSnO_3 thin films. *Ceram. Int.* **46**, 25678–25682 (2020).

55. Prakash, A. et al. Adsorption-controlled growth and the influence of stoichiometry on electronic transport in hybrid molecular beam epitaxy-grown BaSnO_3 films. *J. Mater. Chem. C* **5**, 5730–5736 (2017).
56. Wang, T. et al. Defect-driven localization crossovers in MBE-grown La-doped SrSnO_3 films. *Phys. Rev. Mater.* **1**, 061601 (2017).
57. Giannozzi, P. et al. Advanced capabilities for materials modelling with quantum ESPRESSO. *J. Phys.* **29**, 465901 (2017).
58. van Setten, M. J. et al. The PseudoDojo: training and grading a 85 element optimized norm-conserving pseudopotential table. *Comput. Phys. Commun.* **226**, 39–54 (2018).
59. Jacoboni, C. *Theory of Electron Transport in Semiconductors: A Pathway from Elementary Physics to Nonequilibrium Green Functions* Vol. 165 (Springer Science & Business Media, 2010).

Acknowledgements

This work was supported by the Air Force Office of Scientific Research (AFOSR) through Grant Nos. FA9550-19-1-0245 and FA9550-21-1-0025. Part of this work was supported by the National Science Foundation through DMR-1741801 and partially by the UMN MRSEC program under Award No. DMR-2011401. Parts of this work were carried out in the Characterization Facility, University of Minnesota, which receives partial support from NSF through the MRSEC program. Work at Caltech was supported as follows: J.-J.Z. was supported by the Joint Center for Artificial Photosynthesis, a DOE Energy Innovation Hub, supported through the Office of Science of the U.S. Department of Energy under Award No. DE-SC0004993. M.B. and I.-T.L. were supported by the Air Force Office of Scientific Research through the Young Investigator Program, Grant FA9550-18-1-0280.

Author contributions

T.T. and F.L. grew and structurally characterized samples. T.T. and A.K.R. performed transport measurements, the data from which were analyzed and fit by T.T., A.K.R., I.-T.L., M.B., and B.J. The first-principles calculations were performed by J.-J.Z. and I.-T.L. under the supervision of M.B. SIMS measurements were performed by T.M. and were analyzed by T.M., T.T., and B.J. All authors discussed, interpreted the results, and prepared the manuscript. B.J. coordinated all aspects of the project.

Competing interests

The authors declare no competing interests.

Additional information

Supplementary information The online version contains supplementary material available at <https://doi.org/10.1038/s42005-021-00742-w>.

Correspondence and requests for materials should be addressed to Tristan K. Truttmann, Marco Bernardi or Bharat Jalan.

Peer review information *Communications Physics* thanks the anonymous reviewers for their contribution to the peer review of this work.

Reprints and permission information is available at <http://www.nature.com/reprints>

Publisher's note Springer Nature remains neutral with regard to jurisdictional claims in published maps and institutional affiliations.



Open Access This article is licensed under a Creative Commons Attribution 4.0 International License, which permits use, sharing, adaptation, distribution and reproduction in any medium or format, as long as you give appropriate credit to the original author(s) and the source, provide a link to the Creative Commons license, and indicate if changes were made. The images or other third party material in this article are included in the article's Creative Commons license, unless indicated otherwise in a credit line to the material. If material is not included in the article's Creative Commons license and your intended use is not permitted by statutory regulation or exceeds the permitted use, you will need to obtain permission directly from the copyright holder. To view a copy of this license, visit <http://creativecommons.org/licenses/by/4.0/>.

© The Author(s) 2021